$Mn(Pt_{1-x}Pd_x)_5P$: Isovalent tuning of Mn-sublattice magnetic order

Tyler J. Slade,[1,2,*,†] Ranuri S. Dissanayaka Mudiyanselage,[3,*] Nao Furukawa,[1,2] Tanner R. Smith,[1,2] Juan Schmidt,[1,2] Lin-Lin Wang,[1] Chang-Jong Kang,[4,5] Kaya Wei,[6] Zhixue Shu,[7] Tai Kong,[7] Ryan Baumbach,[6] Gabriel Kotliar,[4] Sergey L. Bud'ko,[1,2] Weiwei Xie,[3,8] and Paul C. Canfield[1,2,‡]

[1]*Ames National Laboratory, US DOE, Iowa State University, Ames, Iowa 50011, USA*
[2]*Department of Physics and Astronomy, Iowa State University, Ames, Iowa 50011, USA*
[3]*Department of Chemistry and Chemical Biology, The State University of New Jersey Rutgers, Piscataway, New Jersey 08854, USA*
[4]*Department of Physics and Astronomy, Rutgers University, Piscataway, New Jersey, 08854, USA*
[5]*Department of Physics, Chungnam National University, Daejeon, 34134, South Korea*
[6]*National High Magnetic Field Laboratory, Tallahassee, Florida, 32310, USA*
[7]*Department of Physics, University of Arizona, Tucson, Arizona 85721, USA*
[8]*Department of Chemistry, Michigan State University, East Lansing, Michigan, 48824, USA*

(Received 28 October 2022; revised 21 February 2023; accepted 24 March 2023; published 21 April 2023)

We report the growth and characterization of $MnPd_5P$, a rare-earth-free ferromagnet, with $T_C \approx 295$ K and planar anisotropy, and conduct a substitutional study with its antiferromagnetic analog $MnPt_5P$. All compounds in the family adopt the layered anti-$CeCoIn_5$-type structure with the space group $P4/mmm$, and EDS and x-ray diffraction results indicate that $MnPt_5P$ and $MnPd_5P$ form a complete solid solution. Based on measurements of the temperature- and field-dependent magnetization and resistance, we construct a temperature-composition (T-x) phase diagram for $Mn(Pt_{1-x}Pd_x)_5P$ and demonstrate that the essentially antiferromagnetic order found in $MnPt_5P$ is extraordinarily sensitive to Pd substitution. At low Pd fractions ($x < 0.010$), the single antiferromagnetic-like transition in pure $MnPt_5P$ splits into a higher-temperature ferromagnetic transition followed first, upon cooling, by a lower temperature ferromagnetic to antiferromagnetic transition and then by a re-entrant antiferromagnetic to ferromagnetic transition at even lower temperatures. The antiferromagnetic region makes up a bubble phase that persists up to $x \approx 0.008$–0.009 for $T \approx 150$ K, with all samples $0 \leqslant x < 0.008$ recovering their initial ferromagnetic state upon further cooling to base temperature. Once $x > 0.010$, $Mn(Pt_{1-x}Pd_x)_5P$ undergoes a only single transition into the ferromagnetic phase. The Curie temperature initially increases rapidly with x, rising from $T_C \approx 197$ K at $x = 0.013$ to a maximum of $T_C \approx 312$ K for $x \approx 0.62$, and then falling back to $T_C \approx 295$ K for pure $MnPd_5P$ ($x = 1.00$). Given that Pt and Pd are isoelectronic, this work raises questions as to the origin of the extreme sensitivity of the magnetic ground state and the nature of the re-entrant ferromagnetism at dilute Pd levels.

DOI: 10.1103/PhysRevB.107.134429

I. INTRODUCTION

Targeted design of tunable magnetic materials is active and key challenge for the materials chemistry and physics community. Achieving this goal necessitates understanding, at a microscopic level, what chemical and structural features underpin the magnetic properties of a given material. Whereas in magnetic semiconductors and insulators, theories based upon superexchange interactions can often provide a satisfactory explanation of the magnetism [1,2], in metallic compounds, it is far more challenging from a theoretical perspective to understand and therefore to predict whether a structure containing transition metals will be paramagnetic, ferromagnetic, or antiferromagnetic [3]. This difficulty is particularly pronounced in the case of low-dimensional and/or itinerant magnetic metals, which show completely different electronic and magnetic properties from magnetic semiconductors [4–9]. With these challenges in mind, detailed studies on isostructural or chemically similar intermetallic compounds with disparate magnetic properties may yield valuable insight into the physical parameters that ultimately determine the magnetism and hopefully provide guidelines for more targeted design of magnetic materials.

The $M(Pt, Pd)_5X$ ($X = P, As$) family is a group of materials that crystallize in the quasi-two-dimensional anti-$CeCoIn_5$-type tetragonal structure with the space group $P4/mmm$ (#123). Whereas members in which M is a late transition metal (Ag, Zn, Cd, Hg) or boron-group element (Al, Ga, In, Tl) have been known for decades [10], we recently discovered several new members where M is a magnetic $3d$ transition metal [11–15]. Despite sharing the same crystal structure, the magnetic properties of the $3d$ metal containing $M(Pt, Pd)_5X$ materials are remarkably diverse. $MnPt_5As$ is a $T_C \approx 280$ K ferromagnet [13], whereas the isovalent $MnPt_5P$ orders antiferromagnetically below $T_N \approx 190$ K (likely with a small ferromagnetic, $q = 0$, component in addition to the predominantly antiferromagnetic order) [11,15]. $FePt_5P$ is an

*These authors contributed equally to this work.
†slade@ameslab.gov
‡canfield@ameslab.gov

itinerant antiferromagnet that undergoes three closely spaced transitions between ≈70–90 K [12,15]. Lastly, $MnPd_5Se$ also shows antiferromagnetic order below $T_N \approx 80$ K, and a spin reorientation is observed upon further cooling below 50 K [14]. The range of properties exhibited by the $M(Pt,\ Pd)_5X$ family suggests that the magnetism in these compounds is extremely sensitive to some combination of chemical composition, electron count, and steric considerations. The case of $MnPt_5P$ is particularly interesting. As noted above, $MnPt_5P$ orders essentially antiferromagnetically, whereas $MnPt_5As$ is a ≈280 K ferromagnet. Very recent work furthermore indicated $MnPd_5P$ exists and manifests ferromagnetic order near room temperature [15], suggesting that both lattice expansion (toward $MnPt_5As$) and contraction (toward $MnPd_5P$) push the antiferromagnetic $MnPt_5P$ toward a ferromagnetic ground state.

In this work, we present a substitutional study between $MnPd_5P$ and $MnPt_5P$ to better characterize the magnetism of the end members and to understand how the initially antiferromagnetic state of $MnPt_5P$ evolves towards ferromagnetism in $MnPd_5P$. Phase and structural analysis with x-ray diffraction and energy dispersive spectroscopy indicate that $MnPt_5P$ and $MnPd_5P$ form a full solid solution of $Mn(Pt_{1-x}Pd_x)_5P$, with no crystallographic evidence for a site preference between Pt and Pd atoms. Magnetization measurements show that the essentially antiferromagnetic state in pure $MnPt_5P$ is extraordinarily sensitive to Pd substitution. At Pd concentrations as low as $x < 0.01$, the single antiferromagnetic transition found for pure $MnPt_5P$ splits into a higher temperature ferromagnetic transition followed first, upon cooling, by a lower temperature ferromagnetic to antiferromagnetic transition and then by a re-entry into the ferromagnetic state at lower temperatures. The antiferromagnetic region makes up a bubble phase that persists up to $x \approx 0.008$–0.009 for $T \approx 150$ K, with all samples $x < 0.008$ recovering their initial ferromagnetic state upon further cooling to base temperature. When $x > 0.010$, $Mn(Pt_{1-x}Pd_x)_5P$ undergoes only a single ferromagnetic transition, where the Curie temperature initially increases with x and is maximized at ≈312 K for $x = 0.62$ Pd before decreasing to ≈295 K in pure $MnPd_5P$. Considering that for $x > 0.01$, the rather gradual and nonmonotonic T_C variation does not track well with lattice parameters, the fantastic sensitivity of the antiferromagnetic phase of $Mn(Pt_{1-x}Pd_x)_5P$ for $x < 0.01$ is remarkable and suggests there is a qualitative change in the material that we suggest may be associated with a change in the Fermi-surface topology, such as a Lifshitz transition. Qualitatively in-line with this proposal, electronic band structure calculations for $MnPt_5P$ indeed show several pockets near the Fermi level which could be altered by Pd substitution. Direct experiments to probe the electronic structure or density of states at the Fermi level are needed to further understand the extraordinary sensitivity of $MnPt_5P$ to Pd alloying.

II. EXPERIMENTAL DETAILS

A. Crystal growth

We prepared and characterized both single crystalline and polycrystalline samples of $MnPd_5P$ and $Mn(Pt_{1-x}Pd_x)_5P$. The $Mn(Pt_{1-x}Pd_x)_5P$ single crystals were grown from $(Pt_{1-x}Pd_x)$-P based solutions as follows [15]: Elemental Mn pieces (Puratronic, 99.98%), Pt powder (Engelhard, 99 + % purity), Pd powder (Engelhard, 99 + % purity), and red P pieces (Alpha-Aesar, 99.99%) were weighed according to nominal compositions of $Mn_9Pt_{71-y}Pd_yP_{20}$ (the actual compositions are given in Table IV in the Appendix) and placed into the bottom of an alumina Canfield crucible set (CCS) [16,17]. The packed CCS was flame sealed into evacuated fused silica ampules that were backfilled with ≈1/6 atm Ar gas. Using a box furnace, the ampules were warmed to 250 °C over 6 h and then to 1180 °C over an additional 8 h. After dwelling at 1180 °C for 6 h, the furnace was gradually cooled to 800 °C (for samples with nominally less than 50% Pd) or to 830 °C (for those with over 50% Pd) over ≈100 h. Upon reaching the desired temperature, the excess liquid phase was decanted by inverting the ampules into a specially designed centrifuge with metal rotor and cups [18]. After cooling to room temperature, the ampules and CCS were opened to reveal clusters of metallic plate-like crystals with typical dimensions of ≈3 mm, and a representative picture of several crystals is shown in the inset to Fig. 1(d).

The polycrystalline samples were prepared from a solid state reaction by sintering pellets with nominal compositions of $Mn(Pt_{1-x}Pd_x)_5P$ ($x = 0.2$, 0.4, 0.5, 0.6, 0.8, and 1). Mn powder (Mangan, 99 + %), Pt powder (BTC, 22 mesh, 99.99%), Pd powder (BTC, 200 mesh, 99.95%) and red P powder (BTC, 100 mesh, 99%) were mixed and ground in $Mn(Pt_{1-x}Pd_x)_5P : P = 1 : 5 : 1$ atomic ratio. The mixture was pressed into a pellet, and the pellet was placed into an alumina crucible and sealed in an evacuated silica tube. The sample tube was then heated to 1050 °C at a rate of 40 °C per hour. After annealing for 2 days at 1050 °C, the samples were slowly cooled to room temperature at the speed of 10 °C per hour. Both the single- and polycrystalline $Mn(Pt_{1-x}Pd_x)_5P$ samples were stable in moist air.

B. Phase and structure determination

Powder x-ray diffraction patterns were obtained using a Rigaku Miniflex-II instrument operating with Cu-$K\alpha$ radiation with $\lambda = 1.5406$ Å ($K\alpha 1$) and 1.5443 Å ($K\alpha 2$) at 30 kV and 15 mA. The samples were prepared by grinding a representative number of crystals (5–10) to a fine powder. To determine the lattice parameters, the powder patterns were refined using the Rietveld method with the GSAS-II software [19]. To obtain a better estimate of the uncertainty in the lattice parameters for samples very dilute in Pd: ($x \leqslant 0.022$), we collected and refined three separate patterns, and used the standard deviations of the refined values of a, c, and V as error bars [see Figs. 1(b)–1(d)]. For samples with $x > 0.022$, the fitting errors from the Rietveld refinements were used as the error bars.

Single-crystal x-ray diffraction (SCXRD) experiments were conducted in a D8 Quest Eco diffractometer with Mo-$K\alpha$ radiation ($\lambda = 0.710\,73$ Å) equipped with Photon II detector. Empirically, we found that the solution grown single crystals of $Mn(Pt_{1-x}Pd_x)_5P$ were not favorable for SCXRD, whereas very small single crystals picked from the sintered pellets (the solid-state reactions) were more suitable and were used for the SCXRD. The samples were mounted on a

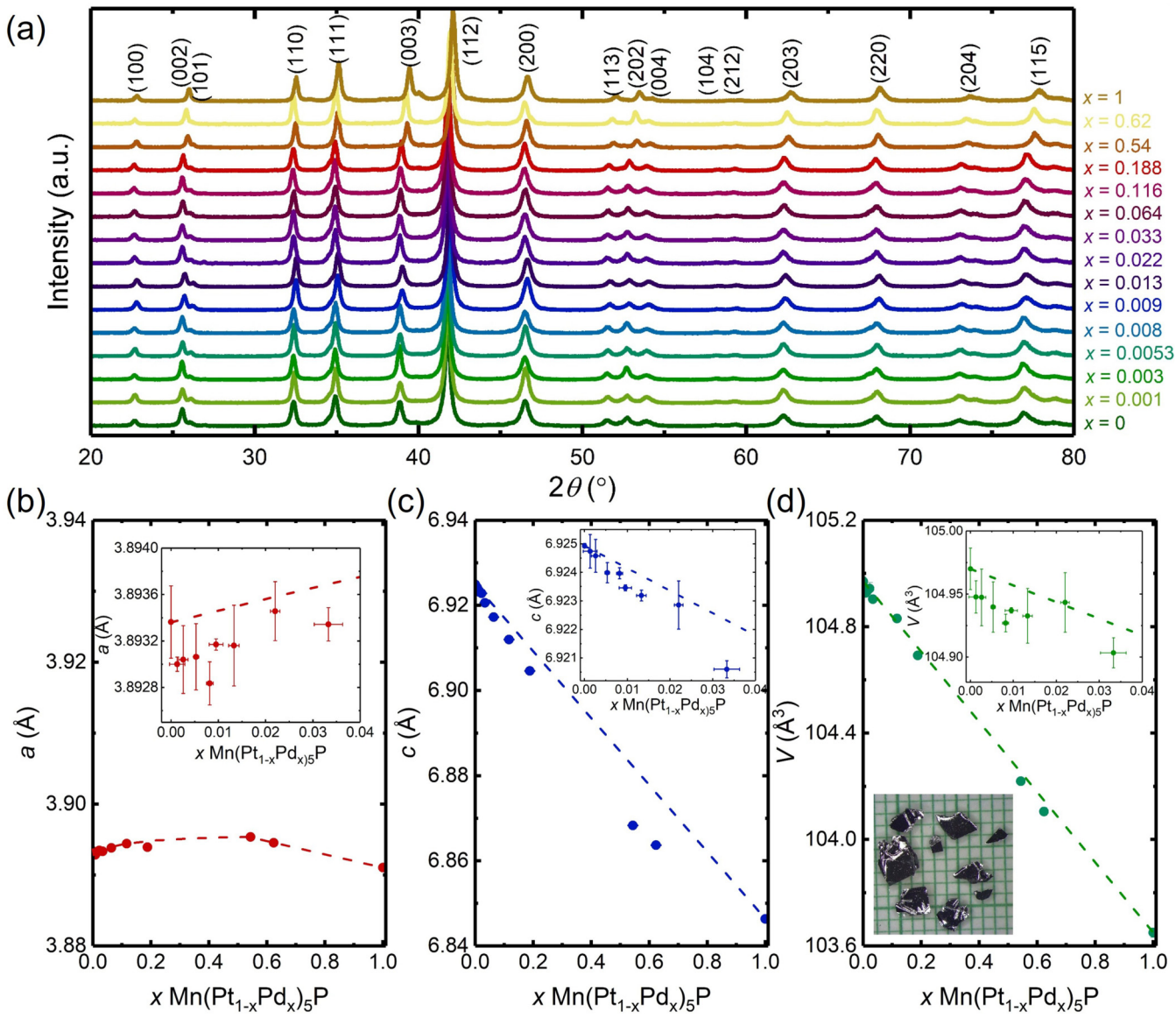

FIG. 1. (a) Powder x-ray diffraction patterns collected from the solution-grown $Mn(Pt_{1-x}Pd_x)_5P$ crystals. The Pd fractions were determined from EDS (see Table IV in the Appendix). Rietveld refined (b) a-lattice parameters, (c) c-lattice parameters, and (d) unit-cell volume V. The dashed line in panel (b) is a guide to the eye connecting $x = 0$ and $x = 1$, and the dashed lines in panels (c) and (d) are linear fits connecting the $x = 0$ and $x = 1$ values of c and V, respectively. The upper insets in panels (b)–(d) show a close-up of the lattice parameters below $x < 0.04$. The lower inset in panel (d) shows several representative crystals on a millimeter grid.

Kapton loop and measured with an exposure time of 10 s per frame scanning 2θ width of 0.5°. Structure refinement was performed in the SHELXTL package using direct methods and full matrix least-squares on F^2 model [20,21]. Anisotropic thermal parameters for all atoms were refined in SHELXTL. The VESTA software was used to plot the crystal structures [22].

C. Scanning electron microscopy and elemental analysis

The Pd concentrations x in the $Mn(Pt_{1-x}Pd_x)_5P$ single crystals were determined by energy dispersive x-ray spectroscopy (EDS) quantitative chemical analysis using an EDS detector (Thermo NORAN Microanalysis System, model C10001) attached to a JEOL scanning-electron microscope (SEM). The compositions of each crystal were measured at several (3–6) different positions on the crystal's face (perpendicular to the c axis), revealing good homogeneity in each crystal. An acceleration voltage of 16 kV, working distance of 10 mm and a takeoff angle of 35° were used for measuring all standards and samples. A pure $MnPt_5P$ single crystal ($x = 0.000$) was used as a standard for Mn, Pt, and P quantification, and a pure $MnPd_5P$ single crystal ($x = 1.000$) was used as a standard for Pd. The spectra were fit using NIST-DTSA II MICROSCOPIUM software [23]. The average compositions and error bars were obtained from these data, accounting for both inhomogeneity and goodness of fit of each spectra. Chemical compositions of the polycrystalline $Mn(Pt_{1-x}Pd_x)_5P$ samples were analyzed using a high-vacuum Zeiss Sigma Field Emission SEM (FESEM) with an Oxford INCA PentaFETx3 energy-dispersive spectroscopy (EDS) system. Spectra were

collected for 100 s from multiple areas of the crystals mounted on a carbon tape with an accelerating voltage of 20 keV.

D. Physical property measurements

For the single crystals, magnetization measurements were performed in a Quantum Design Magnetic Property Measurement System (MPMS-classic) SQUID magnetometer operating in the DC measurement mode. The magnetic measurements were conducted with the field oriented parallel and perpendicular to the c axis, where c is axial direction relative to the plate-like crystals. For measurements with $H \perp c$, the samples were held in place between two plastic straws, and for $H \parallel c$, the samples were sandwiched from above and below between two plastic disks. A small pinhole was poked in the space between the disks to allow for evacuation. In the latter case, a blank background using the bare disks was first measured and the values subtracted.

The temperature dependent resistance of the $Mn(Pt_{1-x}Pd_x)_5P$ single crystals were measured on a Quantum Design Physical Property Measurement System (PPMS) operating in the AC transport mode with an applied current of 3 mA and frequency of 17 Hz. The samples were prepared by cutting the crystals into rectangular bars, and the contacts were made by spot welding 25-μm-thick annealed Pt wire onto the samples in standard four point geometry. After spot welding, a small amount of silver epoxy was painted onto the contacts to ensure good mechanical strength, and typical contact resistances were ≈1 Ω. Unless noted, the data were collected on cooling from 375 to 1.8 K.

E. Computational details

Electronic band structure and density of states for $MnPt_5P$ and $MnPd_5P$ were calculated in density-functional theory (DFT) [24,25] using PBE [26] as the exchange-correlation functional with spin-orbit coupling (SOC) included. All DFT calculations were performed in the Vienna *ab initio* simulation package (VASP) [27,28] with a plane-wave basis set and projector augmented wave method [29]. The kinetic-energy cutoff was 270 eV. We used a Γ-centered Monkhorst-Pack [30] (10 × 10 × 6) k-point mesh with a Gaussian smearing of 0.05 eV for the primitive tetragonal unit cell.

III. RESULTS AND DISCUSSION

A. Phase, composition, and structural analysis

We first analyzed our samples with powder x-ray diffraction (PXRD) and energy dispersive spectroscopy (EDS) to determine the phase and assess the degree of Pd incorporation into the $Mn(Pt_{1-x}Pd_x)_5P$ alloys. Figure 1(a) shows the powder patterns collected for the ground, solution-grown single crystals, and the EDS data are given in Table IV in the Appendix. The PXRD patterns of every sample are in excellent agreement with the anticipated reflections for the $P4/mmm$ structure of $MnPt_5P$ and $MnPd_5P$, and the EDS analysis likewise suggests a monotonic increase in the Pd incorporation into the 1-5-1 matrix as Pt is exchanged for Pd in the starting melts (see Table IV).

TABLE I. Single-crystal structure refinement details for $MnPd_5P$ at 300(2) K.

Refined formula	$MnPd_5P$
F.W. (g/mol)	617.91
Space group; Z	$P4/mmm$; 1
a (Å)	3.899 (2)
c (Å)	6.867 (4)
V (Å^3)	104.42 (9)
θ range (°)	2.966–34.770
No. reflections; R_{int}	578; 0.0609
No. independent reflections	170
No. parameters	12
R_1: wR_2 [$I > 2d(I)$]	0.0509; 0.1204
Goodness of fit	1.282
Diffraction peak and hole (e^-/Å^3)	2.656; −1.863

The lattice parameters determined from Rietveld refinements of the powder patterns are shown in Figs. 1(b) and 1(c). The a-lattice parameter has a very shallow maximum at $x = 0.54$, but overall there is little change in a over the full compositional range. This is contrasted by the c-lattice parameter, which decreases monotonically with a slightly downward bowing from linearity [note the y-axis scales in Figs. 1(b) and 1(c) show that the degree of change in the a-lattice parameter is over an order of magnitude smaller than the change of c). The unit-cell volume V, shown in Fig. 1(d), decreases linearly as the Pd content is raised, closely following Vegard's law for a solid solution between $MnPt_5P$ and $MnPd_5P$.

To provide more detailed structural analysis of $MnPd_5P$ and the $Mn(Pt_{1-x}Pd_x)_5P$ alloys, we conducted single-crystal x-ray diffraction (SCXRD). The resulting crystallographic data, including atomic coordinates, site occupancies, and equivalent isotropic thermal displacement parameters of $MnPd_5P$, are reported in Tables I and II whereas crystallographic information on the $Mn(Pt_{1-x}Pd_x)_5P$ alloys are given in the Appendix in Tables VI and VII. The results confirm that $MnPd_5P$ and the $Mn(Pt_{1-x}Pd_x)_5P$ compounds crystalize in a tetragonal unit cell with the space group of $P4/mmm$, like the previously reported $MnPt_5P$ and $MnPt_5As$. The crystal structure is illustrated in Figs. 2(a) and 2(b) and consists of layered motifs, with alternating layers of $Mn@Pd_{12}$ face sharing polyhedra that span the ab plane and which are separated by P layers along the c axis. Consistent with the powder diffraction data, the single-crystal XRD confirms that the $Mn(Pt_{1-x}Pd_x)_5P$ alloys maintain the parent lattice structure with the Pt and Pd atoms having mixed occupancy on the two

TABLE II. Atomic coordinates and equivalent isotropic displacement parameters of $MnPd_5P$ at 300(2) K. (U_{eq} is defined as one-third of the trace of the orthogonalized U_{ij} tensor (Å^2))

Atoms	Wycoff	Occ.	x	y	z	U_{eq}
Pd1	4i	1	0	1/2	0.2948(1)	0.015(1)
Pd2	1a	1	0	0	0	0.012(2)
Mn3	1c	1	1/2	1/2	0	0.022(2)
P4	1b	1	0	0	1/2	0.016(2)

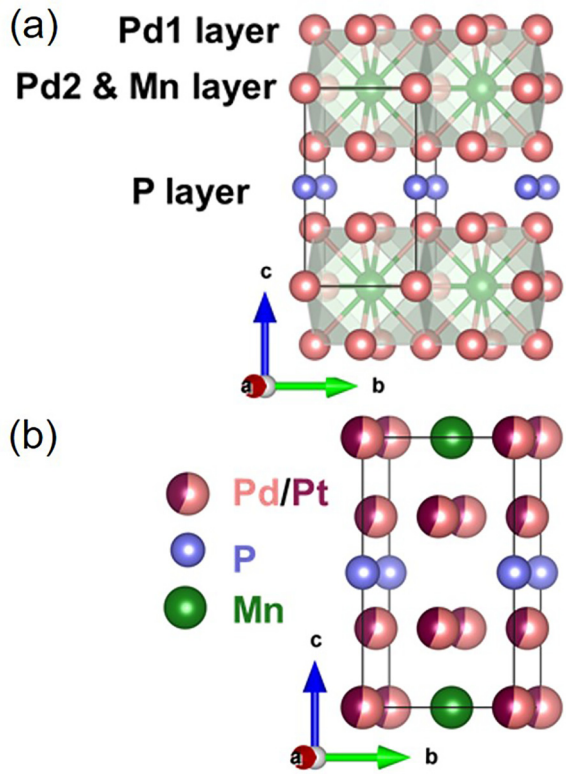

FIG. 2. (a) The crystal structure of $MnPd_5P$ showing $Mn@Pd_{12}$ face sharing polyhedral and P layers (b) Unit cell of $Mn(Pt_{1-x}Pd_x)_5P$ indicating the mixture of Pd and Pt.

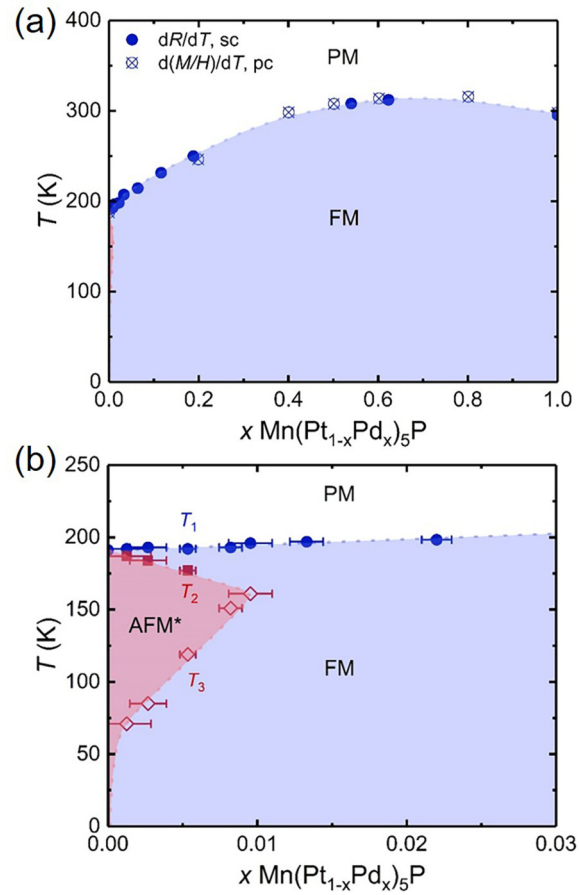

FIG. 3. (a) Full temperature-composition phase diagram for $Mn(Pt_{5-x}Pd_x)_5P$. (b) The low-x region of the phase diagram for $x < 0.03$. The * next to AFM denotes the small ferromagnetic ($q = 0$) component to the primarily antiferromagnetic order in the low-x samples, and the dashed lines are guides to the eye. In panel (a), the closed points represented dated obtained from the single crystals (sc) and the crossed-open points data from the polycrystalline (pc) samples.

atomic sites 1a and 4i as indicated in Fig. 2(b). Details on the Pt and Pd distributions on 1a and 4i sites for each phase are given in Table VII in the Appendix. The SCXRD data may hint that the Pd atoms have a slight preference for occupying the 4i site over the 1a site; however, given the uncertainties in our refinements, this cannot be supported with confidence and our data indicate the Pt and Pd mixing is essentially a solid solution.

B. Temperature-composition magnetic phase diagram of $Mn(Pt_{1-x}Pd_x)_5P$

$MnPt_5P$ enters into a spin-canted antiferromagnetic state at $T_N = 192$ K [11,15], and preliminary data collected on $MnPd_5P$ indicated that this material becomes ferromagnetic near room temperature [15]. To understand how the magnetic state evolves as Pt is replaced with Pd, we conducted temperature and field dependent magnetization and transport measurements on our $Mn(Pt_{1-x}Pd_x)_5P$ single crystals. Using the transition temperatures inferred from the magnetic and transport data, we assembled a temperature-composition (T-x) phase diagram shown in Fig. 3. These results are outlined in detail below.

The temperature dependent resistance and respective derivatives dR/dT are shown in Figs. 4(a)–4(d) and give an initial picture of how the single 192 K transition in pure $MnPt_5P$ evolves upon Pd alloying. As expected, the resistance in each sample has a metallic temperature dependence that decreases with cooling, and the $R(T)$ datasets each show a clear kink followed by a rapid drop at the initial magnetic transition temperature T_1, marking the loss of spin-disorder scattering as the samples enter a magnetically ordered state. The residual resistance ratios, $RRR = R(375\text{ K})/R(1.8\text{ K})$, are shown in Fig. 4(e) and are minimized near $x = 0.5$, as expected for stronger scattering associated with the crystallographically disordered Pt and Pd atoms in the alloys.

Based on the maxima in derivatives of the $R(T)$ data, we estimated the magnetic transition temperatures in each sample [31]. At low Pd fraction [Fig. 4(b)], the initial 192 K transition (T_1) for $x = 0$ splits into two transitions, where T_1 increases with x, and the second transition (T_2) is suppressed from $\approx$187 K at $x = 0.0013$ to $\approx$177 K at $x = 0.0053$. Further cooling reveals a third transition (T_3) that increases with Pd alloying from $\approx$71 K for $x = 0.0013$ to 160 K at $x = 0.009$. T_3 is hysteretic between warming and cooling, implying it is first order [see the zoomed view in Fig. 4(f)]. Only two transitions are observed when the Pd level reaches $x = 0.008$ and $x = 0.009$, which is likely due to the close proximity of T_2 and T_3 at these compositions. Beyond $x > 0.01$, only a

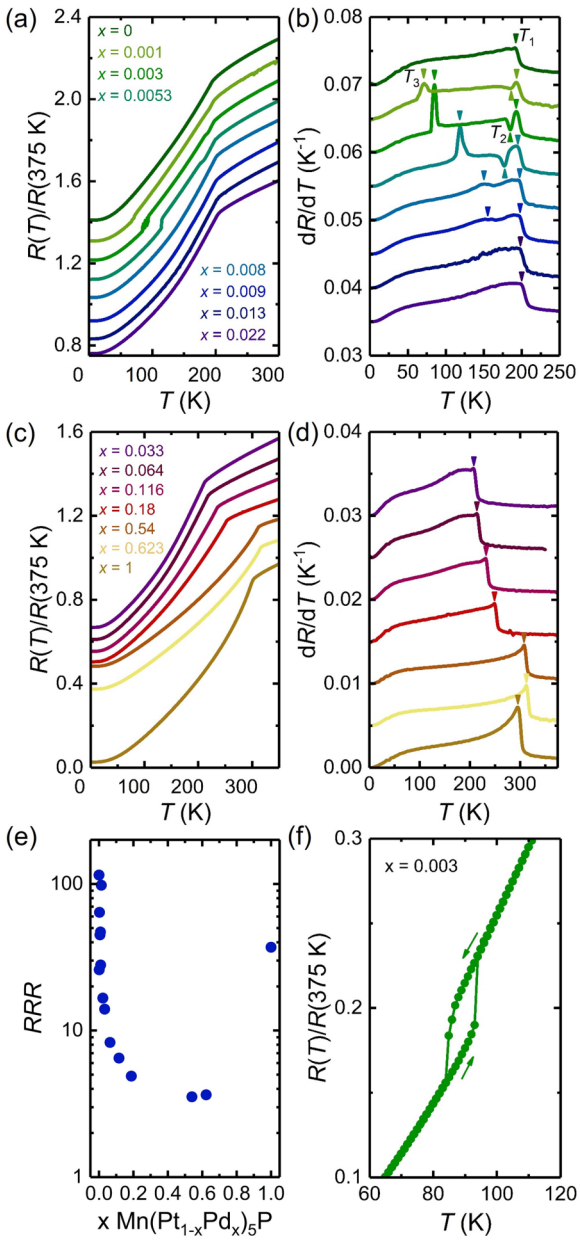

FIG. 4. (a) Temperature-dependent resistance data for $Mn(Pt_{1-x}Pd_x)_5P$, $x \leqslant 0.022$ single crystals with the data normalized to $R(375\ \mathrm{K})$. For clarity, the $R(T)$ curves are each offset by 0.1. (b) Derivatives of the datasets in panel (a). The peaks were used to determine transition temperatures and are marked with arrows [31]. Panels (c) and (d) are the respective $R(T)/R(375\ \mathrm{K})$ and dR/dT data for $x \geqslant 0.033$. (e) Residual resistance ratios (RRR) for each sample. (f) Close-up of the $R(T)$ data near T_3 for the $x = 0.003$ sample showing hysteresis on increasing and decreasing temperature sweeps.

single transition is observed, which increases rapidly with Pd substitution and is maximized at ≈312 K for $x = 0.62$ before falling back to 295 K for pure $MnPd_5P$.

Temperature dependent magnetization (M/H) collected at $H = 1$ kOe for the $Mn(Pt_{1-x}Pd_x)_5P$ single crystals is presented in Figs. 5(a) and 5(b). Lower field M/H data obtained at $H = 50$ Oe is shown in Figs. 5(c) and 5(d). The M/H results indicate the *ab* plane ($H \perp c$ orientation) is the easy direction for all samples, which is confirmed by the field-dependent magnetization isotherms shown below in Figs. 6 and 7. At high temperatures above the respective transitions, M/H is Curie-Weiss like for all samples, as shown in Fig. 10 in the Appendix. As summarized in Table III, the paramagnetic Weiss temperatures track well with the initial transitions T_1, and the effective moments remain approximately constant across the series, with values of $(5.8 \pm 0.2)\mu_B$, very close to the theoretical value of $5.9\mu_B$ expected for Mn^{2+} moments.

TABLE III. Paramagnetic Weiss temperatures, High temperature effective moments, 2 K saturated moments (measured at 50 kOe), and Rhodes-Wohlfarth ratios (q_c/q_s) of all $Mn(Pt_{1-x}Pd_x)_5P$ single-crystal samples.

x	Θ (K)	μ_{eff} (μ_B/f.u.)	μ_{sat} (μ_B/f.u.)	q_c/q_s
0	206(2)	5.85(6)	4.49(4)	1.32(2)
0.001(1)	206(6)	5.9(1)	4.9(1)	1.23(4)
0.003(1)	208(3)	5.85(6)	4.65(4)	1.28(2)
0.0053(5)	209(2)	5.91(5)	4.74(4)	1.27(2)
0.0082(7)	209(5)	6.0(1)	4.7(1)	1.29(4)
0.009(1)	210(3)	5.93(7)	4.77(5)	1.26(2)
0.013(2)	211(3)	5.86(7)	4.71(5)	1.26(2)
0.022(1)			4.61(6)	
0.033(3)	219(7)	5.8(2)	4.65(3)	1.27(4)
0.064(3)	225(4)	5.75(8)	4.32(6)	1.35(3)
0.116(5)	238(2)	5.97(4)	4.74(2)	1.28(1)
0.188(5)	259(2)	5.61(4)	4.40(3)	1.29(1)
0543(4)	313(4)	5.75(5)	4.53(2)	1.26(2)
0.623(4)	290(5)	5.65(8)	4.54(6)	1.26(2)
1	257(2)	5.58(3)	4.0(4)	1.29(1)

When the magnetic field is applied within the easy *ab* plane, dilute Pd substitution ($x < 0.01$) causes the initially narrow, antiferromagnetic-like, peak observed at 192 K for pure $MnPt_5P$ to shift to higher temperatures and substantially broaden as x increases [see 50 Oe data in Fig. 5(c)], forming a plateau-like maxima centered near ≈180 K. These features closely correspond to the evolution of T_1 and T_2 in the resistance data [see Fig. 4(b)]. Likewise, upon Pd substitution, the weak upturn in M/H below 100 K observed in $MnPt_5P$ becomes a sharp increase reminiscent of ferromagnetic ordering. This ferromagnetic-like upturn tracks well with T_3 in the resistance data and moves to higher temperatures as x increases, eventually merging with T_2 such that by $x = 0.008$, only two features are observed in the 50 Oe M/H data, an initial ferromagnetic-like transition at ≈193 K, followed by a second, subtle, increase beginning at ≈150 K. Above $x > 0.010$, only a single ferromagnetic transition is observed, and the Curie temperature increases with Pd alloying to a maximum at 312 K for $x = 0.62$ before falling gradually back to ≈295 K for pure $MnPd_5P$.

Using the transitions identified in the temperature dependent M/H and $R(T)$ data discussed above, we can delineate regions of the T-x phase diagram shown in Fig. 3. We find that the initial transition at 192 K in pure $MnPt_5P$ splits into two transitions, T_1 and T_2, upon even minute levels of Pd substitution. T_1 appears to be ferromagnetic and increases with x to a maximum at 312 K for $x = 0.62$, whereas T_2 decreases

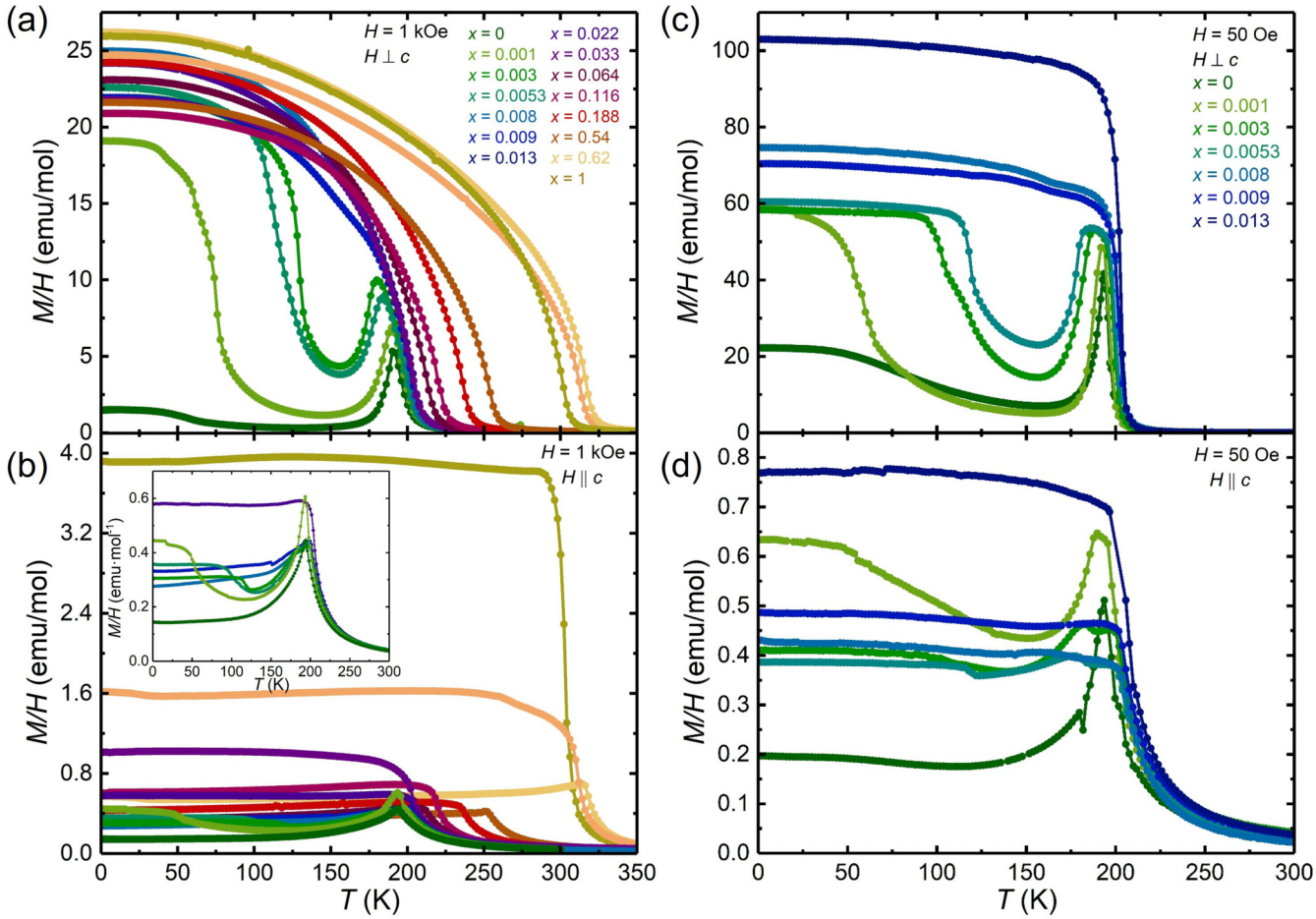

FIG. 5. Temperature dependence of M/H for all $Mn(Pt_{1-x}Pd_x)_5P$ single crystals. All measurements where field-cooled. (a) Data for $H \perp c$ and (b) $H \parallel c$ in a $H = 1$ kOe field. Panels (c) and (d) are the same for low x $Mn(Pt_{1-x}Pd_x)_5P$ with $x < 0.02$ and $H = 50$ Oe. The inset in panel (b) shows a closer view of the $H \parallel c$ data for samples with $x < 0.022$.

gradually with x. The low-x samples show a third, lower temperature transition T_3 that increases with x and intersects T_2 at approximately $x \approx 0.008$–0.009, such that T_2 and T_3 delineate a "bubble region" on the phase diagram that extends out to $x \approx 0.009$.

To better determine the type of order found in each region of the phase diagram, we obtained magnetization isotherms at salient temperatures for samples with different values of x. Anisotropic $M(H)$ data are given in Figs. 6(a) and 6(b) for $x = 0.0053$, which is taken as representative for the low-x samples. Depending on the temperature, the $H \perp c$ isotherms show either rich metamagnetism or rapid saturation at maximum values of $\approx 4.6\mu_B$ (the values of μ_{sat} are summarized in Table III). On the other hand, the magnetization in the $H \parallel c$ orientation is an order of magnitude weaker with essentially linear behavior and little or no hints of saturation up to at least 50 kOe. The anisotropic $M(H)$ results in Figs. 6(a) and 6(b) confirm that the *ab* plane is the easy direction, as inferred from the M/H data.

The magnetization isotherms measured in the easy $H \perp c$ direction allow for clear assignment of each region of the phase diagram. For pure $MnPt_5P$ [Fig. 6(c)], the $M(H)$ curves show a series of metamagnetic transitions that shift to lower field as the temperature is lowered, indicating antiferromagnetic order. As outlined in our prior work [15], there is a small ferromagnetic ($q = 0$) component to the order in $MnPt_5P$, but the observance of metamagnetism at all temperatures below T_N indicates the ground state remains primarily antiferromagnetic down to at least 2 K [we use * in Fig. 3(b) to denote the ferromagnetic component to the otherwise primarily antiferromagnetic state]. This is consistent with the $R(T)$ data for $MnPt_5P$ showing only a single 192 K transition. This said, the very low metamagnetic field, which decreases with decreasing temperature rather than the more standard increasing with decreasing temperature, strongly suggests a close energetic proximity to an ordered state with a larger ferromagnetic component.

Upon introduction of Pd, the $M(H)$ isotherms measured above the "bubble" region of the phase diagram, at temperatures between T_1 and T_2, show a swift rise in M at low field followed by saturation at above ≈ 1 kOe, implying that T_1 is a ferromagnetic transition [see 185 K data in Fig. 6(a) and 190 K data in Figs. 6(d) and 6(e)]. Within the bubble, between T_2 and T_3, the $M(H)$ curves all show metamagnetic transitions that generally move to lower fields as the temperature is lowered (for a given value of x). Likewise, the $M(H)$ datasets all show a small but measurable low-field saturation below ≈ 0.2 kOe. Together, this information suggests

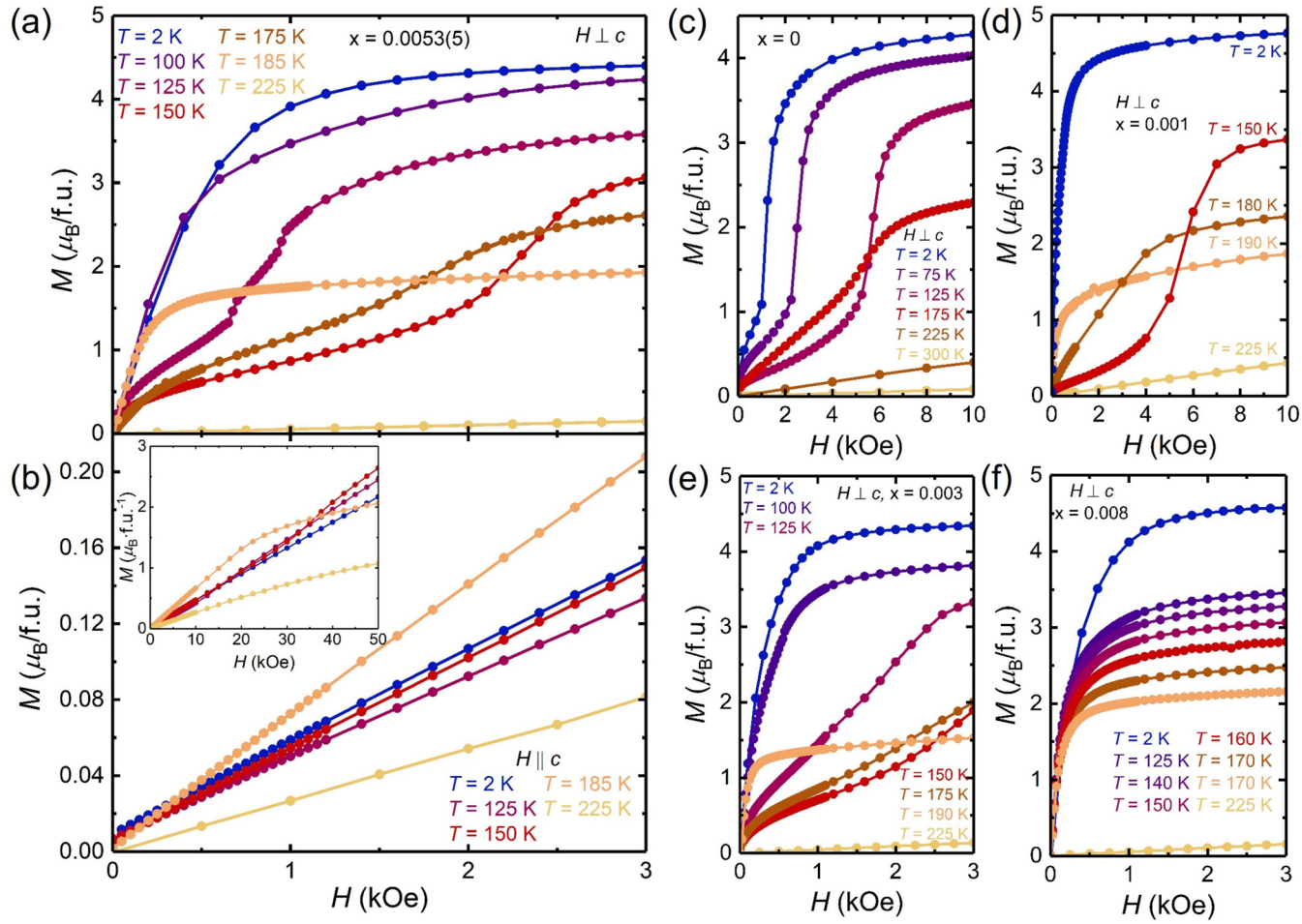

FIG. 6. (a) Field dependent magnetization isotherms for $x = 0.0053(5)$ $Mn(Pt_{1-x}Pd_x)_5P$ measured in the easy direction ($H \perp c$) and (b) hard direction ($H \parallel c$). The inset in panel (b) shows the data up to 50 kOe. (c)–(f) show the $H \perp c$ magnetization isotherms for (c) $x = 0$, (d) $x = 0.001$, (e) $x = 0.003$, (f) $x = 0.008$. Note that the x-axis scale for panels (c) and (d) extends to 10 kOe to observe the metamagnetic transitions.

that the bubble phase is the same spin-canted AFM* state found in pure $MnPt_5P$. Below T_3, the $M(H)$ isotherms for Pd containing samples again are characteristic ferromagnetic behavior, with a rapid increase in M at low field followed by saturation at $\approx 4.6\mu_B$/f.u. Once x reaches 0.008 [Fig. 6(f)], the magnetization isotherms show ferromagnetic behavior at all temperatures, consistent with the temperature dependent data that show T_2 and T_3 essentially merging into a single transition at this level of Pd substitution.

Figure 7 displays the anisotropic magnetization collected at 2 K for samples with $x > 0.01$. In agreement with the temperature dependent M/H data, the $M(H)$ isotherms show classic easy-plane ferromagnetic behavior at all temperatures below T_1. At 2 K, the saturated moments μ_{sat}, summarized in Table III, have essentially constant values of $\approx 4.6\mu_B$, which is not far from the $5\mu_B$ expected for Mn^{2+} moments. As there is no systematic trend across the series, the approximately $\pm 0.3\mu_B$ variance of saturated moments likely comes from a combination of weighing errors, uncertainty in x (and molar mass), sample orientation etc., and do not represent any real change in μ_{eff}. Because both the saturated and effective moments are close to the theoretical values anticipated for Mn^{2+}, we can conclude that the magnetism in $Mn(Pt_{1-x}Pd_x)_5P$ is primarily local moment like, as is commonly observed for Mn containing compounds. Local moment magnetism is supported by the relatively small Rhodes-Wohlfarth ratios (q_c/q_s), listed in Table III, which are expected to be close to unity for local moment systems [4].

The $M(H)$ curves have very small ($\approx$10–20 Oe), almost negligible, hysteresis on raising and lowering the field, implying that the ferromagnetism in $Mn(Pt_{1-x}Pd_x)_5P$ single crystals is very soft. Moreover, the $M(H)$ results show that the $Mn(Pt_{1-x}Pd_x)_5P$ samples have relatively strong planar magnetic anisotropy. Anisotropy fields H_A estimated by extrapolating the tangents of the $H \perp c$ and $H \parallel c$ datasets decrease monotonically as the Pd fraction rises, from $\approx$108 kOe for $x = 0.022$ Pd to $\approx$10 kOe in $MnPd_5P$, which likely reflects the decreasing strength of spin-orbit coupling accompanying substitution of the Pt with the smaller Z Pd.

C. Discussion

The phase diagrams delineated by our magnetic and transport measurements and shown in Fig. 3 have two primary points of interest. First, the re-entrant ferromagnetism observed at low Pd substitution is unusual. As shown in

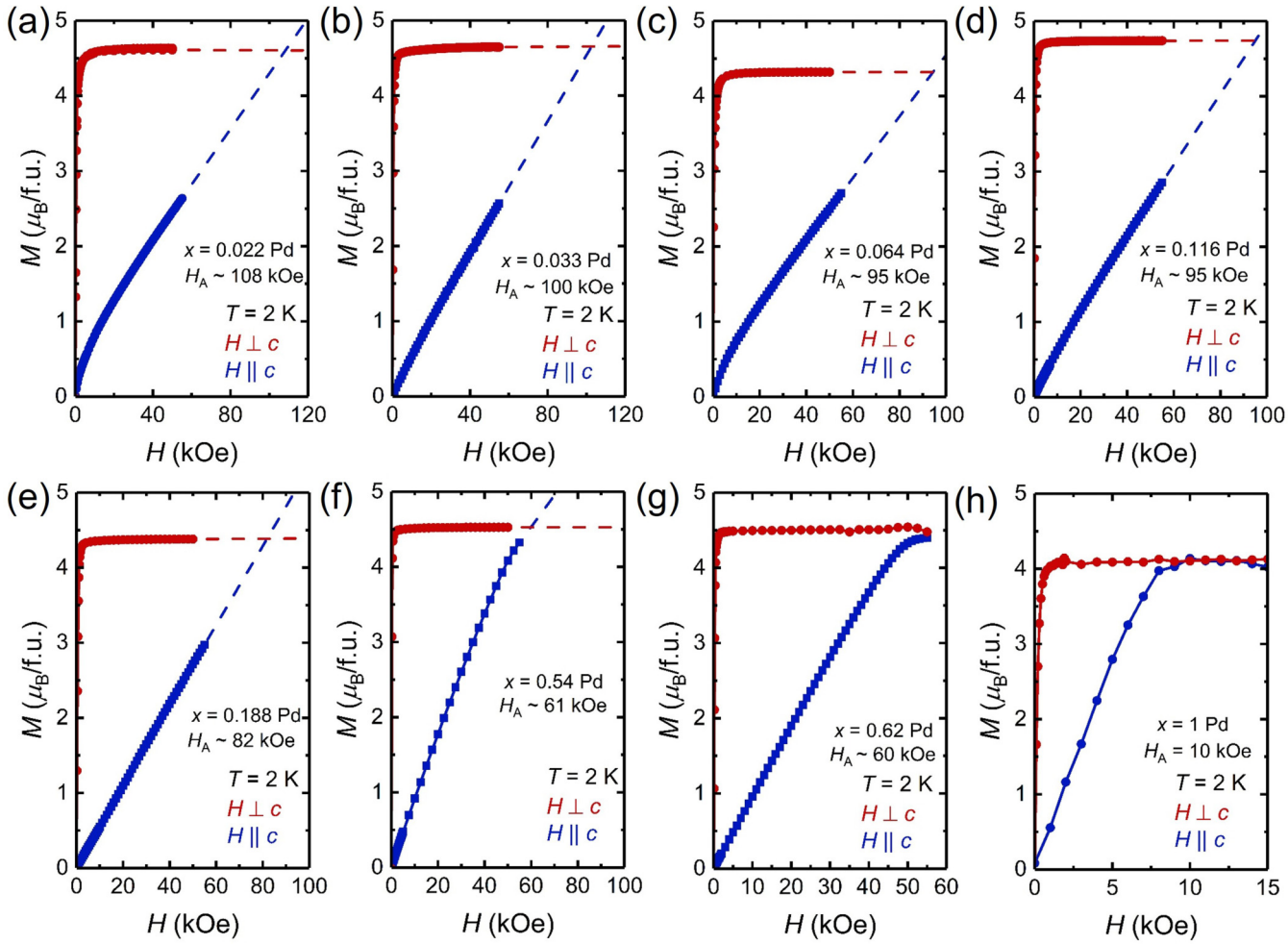

FIG. 7. Field-dependent magnetization isotherms measured at 2 K for all Pd containing $Mn(Pt_{1-x}Pd_x)_5P$ ($x \geqslant 0.022$) single crystals. The small degree of nonlinearity observed at low fields for $x = 0.022$ and $x = 0.064$ Pd likely arise from slight misorientations of the samples. The dotted lines show the extrapolation of the tangents used to estimate the anisotropy fields H_A.

Fig. 3(b), at very low, essentially homeopathic levels of Pd $x < 0.01$, the single transition in $MnPt_5P$ splits into two transition that separate as the Pd level increases. The first transition is ferromagnetic, and the lower transition makes up an antiferromagnetic "bubble" that extends from pure $MnPt_5P$ to $x \approx 0.008$–0.009 and below which the original ferromagnetic order is recovered on cooling. Re-entrant phase transitions, in which a high-temperature phase with higher symmetry is recovered on cooling, are relatively rare [32–37], and are typically observed when multiple degrees of freedom compete with each other on cooling. With this in mind, it would be useful to conduct low temperature x-ray diffraction measurements on samples with $x < 0.01$ to determine if there are any structural distortions associated with the antiferromagnetic transition T_2, or the re-entrant ferromagnetic transition T_3.

Second, the sensitivity of $MnPt_5P$ to Pd substitution is remarkable, as only the small, isovalent, perturbation of $x \approx 0.013$ Pd substitution on the Pt sites is sufficient to produce a change from antiferromagnetic to purely ferromagnetic order. One possible explanation for the sensitivity of $MnPt_5P$ to Pd substitution is a Lifshitz type transition where the Fermi-surface topology abruptly changes, i.e., small pockets appear and/or disappear with small Pd substitution. Such an electronic transition will lead to changes in the density of states (DOS) at the Fermi energy as well as changes in the generalized electronic susceptibility, $\chi(q)$, which governs whether the magnetic order is anti- or ferromagnetic. Because a change in electronic structure could affect the crystal structure (as well as the magnetic interactions), it is worth noting that nonmonotonic changes in the a-lattice parameter and unit-cell volume are possibly detected at room temperature over essentially the same range of low x [see the insets to Figs. 1(b)–1(d)] that the antiferromagnetic bubble is observed; although the error bars associated with our refinements leave this possible correlation at the edge of resolvability.

To assess the possibility of a change in Fermi-surface topology, we calculated electronic band structures for nonmagnetic $MnPt_5P$ and $MnPd_5P$. The band structures are displayed in Fig. 8, where the green shading represents the projection of Mn-3d orbitals to the electronic states. As expected, the calculations indicate both $MnPt_5P$ and $MnPd_5P$ are metals, with multiple well-dispersed bands crossing the Fermi energy (E_F). In both compounds, most of the bands near E_F are composed of Mn-3d based states. Most importantly, the band structure for pure $MnPt_5P$ has several bands that graze, or come very close to E_F at the M, R, and A points

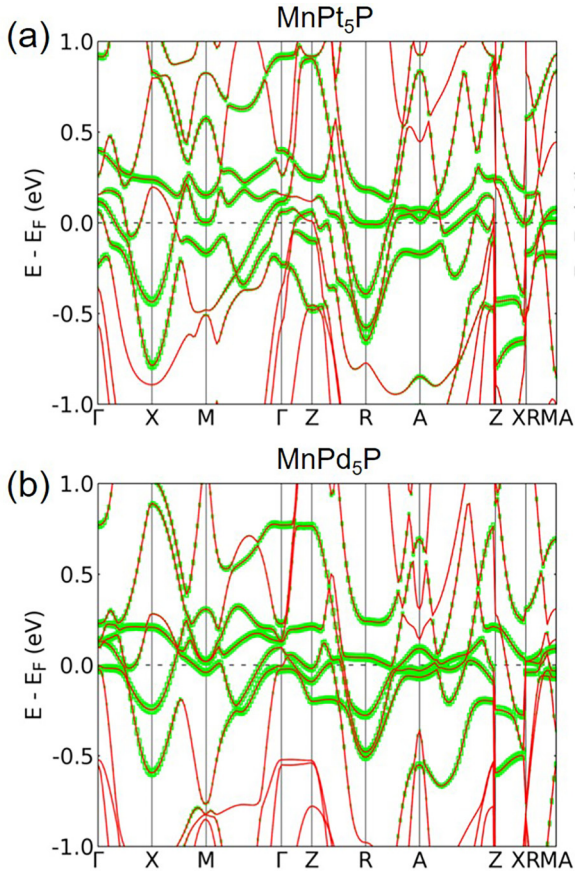

FIG. 8. Electronic band structures calculated for (a) $MnPt_5P$ and (b) $MnPd_5P$. The green shading represents the relative projection of Mn-3*d* orbitals to the electronic bands.

in the Brillouin zone, as well as a Dirac-like set of bands along X–M. In $MnPd_5P$, the flat-band sections near the M and R points move above E_F, and the band along the X–M direction also moves up in energy. Furthermore, new flat-band sections appear near E_F in $MnPd_5P$ along the Γ–X and A–Z directions. Admittedly, comparison of the end members $MnPt_5P$ and $MnPd_5P$ represents an extreme perturbation in reference to the $x \approx 0.013$ needed to stabilize purely ferromagnetic order in $Mn(Pt_{5-x}Pd_x)_5P$; however, the calculations do show that $MnPt_5P$ has multiple pockets very near E_F that are substantially changed in $MnPd_5P$, suggesting a Lifshitz transition is at least plausible in $Mn(Pt_{5-x}Pd_x)_5P$. Subsequent measurements that directly probe the electronic states at E_F, such as the thermopower and Hall effect, would be needed to explore and test this proposal.

IV. SUMMARY AND CONCLUSIONS

We determined that ferromagnetic $MnPd_5P$ adopts the anti-$CeCoIn_5$ structure with the space group $P4/mmm$ and conducted a detailed substitutional study with its isostructural antiferromagnetic analog $MnPt_5P$. EDS and x-ray diffraction data support the formation of a full $Mn(Pt_{1-x}Pd_x)_5P$ solid solution that maintains the tetragonal anti-$CeCoIn_5$ structure. The magnetic data show that the primarily antiferromagnetic state in pure $MnPt_5P$ is extremely sensitive to Pd substitution, and as little as $x > 0.010$ Pd stabilizes purely ferromagnetic order. At low $x < 0.010$, $Mn(Pt_{1-x}Pd_x)_5P$ shows unusual re-entrant ferromagnetism. Here, the single antiferromagnetic transition in $MnPt_5P$ splits into a higher temperature ferromagnetic transition and lower temperature ferromagnetic-to-antiferromagnetic transition. The antiferromagnetic region forms a bubble in the T–x phase diagram that persists up to $x \approx 0.008$–0.009, and for which further cooling recovers the ferromagnetic state. We speculate that the fantastic sensitivity of $MnPt_5P$ to isovalent Pd substitution may involve a change in Fermi-surface topology accompanying dilute Pd incorporation, resulting in a change of $\chi(q)$ and the associated magnetic interactions. Electronic band-structure calculations indicate pure $MnPt_5P$ has several pockets close to the Fermi level that could be involved in such a transition. Beyond $x > 0.010$, the ferromagnetic Curie temperature is substantially enhanced with Pd incorporation to $\approx$312 K at $x = 0.62$ before falling back to 295 K in pure $MnPd_5P$. All $Mn(Pt_{1-x}Pd_x)_5P$ samples have strong magnetic anisotropy in which the *ab* plane is the easy direction, and the anisotropy field decreases from $\approx$108 kOe for $x = 0.022$ Pd to $\approx$10 kOe for $MnPd_5P$, likely a result of reduced spin-orbit coupling.

ACKNOWLEDGMENTS

Work at Ames National Laboratory (T.J.S., N.F., T.R.S., J.S., L.L.W., S.L.B., and P.C.C.) was supported by the U.S. Department of Energy, Office of Science, Basic Energy Sciences, Materials Sciences and Engineering Division. Ames National Laboratory is operated for the U.S. Department of Energy by Iowa State University under Contract No. DE-AC02-07CH11358. T.J.S. and L.L.W. were supported by the Center for Advancement of Topological Semimetals (CATS), an Energy Frontier Research Center funded by the U.S. Department of Energy Office of Science, Office of Basic Energy Sciences, through the Ames National Laboratory under its Contract No. DE-AC02-07CH11358 with Iowa State University. The work at Rutgers is supported by Beckman Young Investigator award. C.-J.K. and G.K. were supported by the U.S. Department of Energy, Office of Science (Basic Energy Science) as a part of the Computational Materials Science Program through the Center for Computational Design of Functional Strongly Correlated Materials and Theoretical Spectroscopy under DOE Grant No. DE-FOA-0001276. C.-J.K. also acknowledges support by NRF Grant No. 2022R1C1C1008200. A portion of this work was performed at the National High Magnetic Field Laboratory, which is supported by National Science Foundation Cooperative Agreement No. DMR-1644779 and the State of Florida. R.B. acknowledges support from NSF-DMR-1904361.

APPENDIX

1. EDS analysis of $Mn(Pt_{1-x}Pd_x)_5P$

Table IV lists the nominal compositions $Mn_9Pt_{71-y}Pd_yP_{20}$ used for the growth of $Mn(Pt_{1-x}Pd_x)_5P$ single crystals and the corresponding values of x determined by EDS from each batch. Note that starting compositions do not correspond to exact $Mn(Pt_{1-x}Pd_x)_5P$ stoichiometry (i.e., $y \neq x$) because the intention for solution growth is to intersect the liquidus

TABLE IV. Chemical compositions determined from EDS analysis for the solution-grown single crystals of $Mn(Pt_{1-x}Pd_x)_5P$. The nominal compositions used for the growth were $Mn_9Pt_{71-y}Pd_yP_{20}$, and we also give the nominal Pd fraction (x) in each. The EDS values of x represent the averages of 3–6 scans on each sample and the error bars were obtained considering both the EDS fitting errors and standard deviations of each measurement (see text).

Nominal y	Nominal x	EDS x $Mn(Pt_{1-x}Pd_x)_5P$
0.25	0.0035	0.00013 ± 0.001
0.5	0.0070	0.003 ± 0.001
1	0.014	0.0053 ± 0.0005
1.5	0.021	0.0082 ± 0.0007
1.75	0.025	0.009 ± 0.001
2.25	0.032	0.013 ± 0.002
3	0.042	0.022 ± 0.001
6	0.0845	0.033 ± 0.003
9	0.13	0.0635 ± 0.003
16	0.225	0.116 ± 0.005
23	0.32	0.188 ± 0.005
47	0.66	0.543 ± 0.004
50	0.70	0.623 ± 0.004

surface for crystallization of $Mn(Pt_{1-x}Pd_x)_5P$ on cooling, not to be directly "on-line." Table V gives the same information for the polycrystalline samples obtained from solid-state reactions. The values of x are the average of multiple scans obtained on each sample and the error bars were determined either by the standard deviations or the EDS fitting error (the fitting error was only used for $x = 0.0001$). We calculated x relative to the total amount of Pt and Pd detected in each sample, i.e., $x = f_{Pd}/(f_{Pt} + f_{Pd})$ where f_{Pt} (f_{Pd}) represent the quantity of Pt (Pd) found in each sample. For both the solution-growth single crystals and polycrystalline samples, we observe a monotonic enrichment of the EDS Pd fraction as the starting growth compositions become richer in Pd. For the single-crystalline sample with nominal $y = 0.25$ and EDS $x = 0.000\,13$, the Pd fraction is under the detection limit of our instrument (the fitting errors to the EDS spectra were ≈10 times greater than the detected quantity of Pd). This is unsurprising given the extremely dilute quantity added to the initially melt ($y = 0.25$, which is ≈0.35% Pd relative to the total quantity of Pt and Pd); however, the significant differences in the magnetic and transport properties between this sample and those of pure $MnPt_5P$ imply very small but finite Pd incorporation (see Figs. 5 and 6 in the main text).

TABLE V. Chemical compositions determined from EDS analysis for the polycrystalline samples of $Mn(Pt_{1-x}Pd_x)_5P$.

Nominal $x$$Mn(Pt_{1-x}Pd_x)_5P$	EDS $x$$Mn(Pt_{1-x}Pd_x)_5P$
0.2	0.188(5)
0.4	0.39(2)
0.5	0.502(5)
0.6	0.589(3)
0.8	0.81(1)

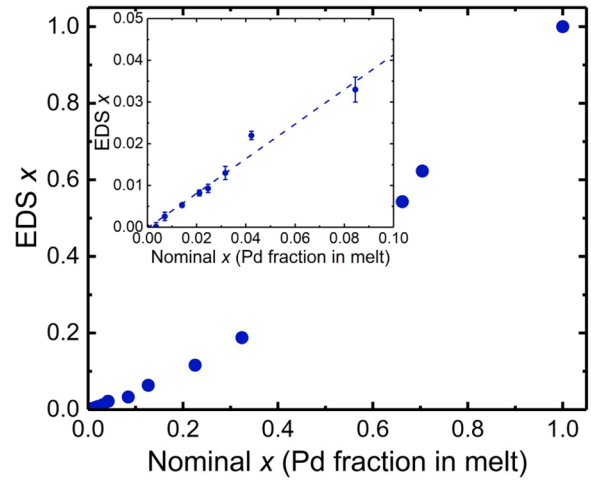

FIG. 9. EDS values of x Pd in $Mn(Pt_{1-x}Pd_x)_5P$ compared with the nominal x added to the starting crystal-growth compositions. The inset shows a closeup of the low-x data, and the dashed line is a linear fit to the data up to nominally $x = 0.0845$.

Given the detected Pd in this sample is below the resolution of our instrument, to estimate the Pd fraction, we extrapolated the linear trend between nominal and EDS values of x to nominally $x = 0.0035$ (see the inset to Fig. 9), which gives an estimate of $x = 0.0013$ for the most dilute sample.

2. Crystallographic information for $Mn(Pt_{1-x}Pd_x)_5P$

Table VI gives the refinement information and statistics for the single crystal XRD refinements of $Mn(Pt_{1-x}Pd_x)_5P$ samples. The single crystals used for these measurements were picked from the sintered pellets (solid-state reactions). The atomic positions and isotropic displacement parameters are listed in Table VII. The results indicate that $MnPd_5P$ and the $Mn(Pt_{1-x}Pd_x)_5P$ compounds all adopt the layered tetragonal ($P4/mmm$) anti-$CeCoIn_5$ type structure. The single-crystal XRD refinements support mixed occupancy between Pt and Pd on the two atomic sites $1a$ and $4i$, indicating the formation of a $Mn(Pt_{1-x}Pd_x)_5P$ solid solution. As shown in Table VII, the Pd atoms may have a slight preference for occupying the $4i$ site over the $1a$ site; however, given the uncertainties of our experiments we are not able to confidently assert at site preference for the Pt or Pd atoms.

3. Additional magnetic data for $Mn(Pt_{1-x}Pd_x)_5P$ single crystals

Figure 10 shows the inverse $(M/H)^{-1}$ of the polycrystalline averaged M/H datasets for each $Mn(Pt_{1-x}Pd_x)_5P$ sample. Here $M/H_{PC} = 1/3M/H_{\|} + 2/3M/H_{\perp}$, where $M/H_{\|}$ and $M/H_{\perp}$ are the respective $H \parallel c$ and $H \perp c$ datasets shown in Fig. 5(a) and 5(b). The $(M/H)^{-1}$ curves all show Curie-Weiss like behavior at high temperatures, with linear M/H^{-1} above the respective transition temperatures. We therefore fit the high-temperature data to the Curie-Weiss law $M/H = C/(T - \Theta)$, where C is the Curie constant and Θ the Weiss temperature. The estimated values of Θ, listed in Table III, track reasonably well with the Curie temperatures and are positive for all samples, consistent with the observed

TABLE VI. Single-crystal structure refinement information for $Mn(Pt_{1-x}Pd_x)_5P$ at 300(2) K. (The standard deviations are indicated by the values in parentheses.) The single crystals used for data collection and refinement were picked from the sintered pellets.

Loaded composition	$MnPd_5P$	$Mn(Pt_{0.2}Pd_{0.8})_5P$	$Mn(Pt_{0.4}Pd_{0.6})_5P$	$Mn(Pt_{0.5}Pd_{0.5})_5P$	$Mn(Pt_{0.6}Pd_{0.4})_5P$
Refined Formula	$MnPd_5P$	$Mn(Pt_{0.172(4)}Pd_{0.828(4)})_5P$	$Mn(Pt_{0.454}Pd_{0.546})_5P$	$Mn(Pt_{0.48}Pd_{0.52})_5P$	$Mn(Pt_{0.58}Pd_{0.42})_5P$
F.W. (g/mol)	617.91	694.18	819.24	848.5	875.11
Space group; Z	$P4/mmm$; 1	$P4/mmm$; 1	$P4/mmm$; 1	$P4/mmm$; 1	$P4/mmm$; 1
a (Å)	3.899(2)	3.894(1)	3.887(2)	3.888 (2)	3.901(3)
c (Å)	6.867(4)	6.855(1)	6.853(2)	6.861(2)	6.892(4)
V (Å^3)	104.42(2)	103.93(2)	103.54(4)	103.73(5)	104.93(11)
θ range (°)	2.966–34.770	5.236–34.828	5.246–34.892	2.969–3.874	5.919–34.646
No. reflections; R_{int}	578; 0.0609	1397; 0.0293	999; 0.0444	904; 0.0549	214; 0.0233
No. independent reflections	170	173	166	167	94
No. parameters	12	14	14	14	14
R_1: wR_2 ($I > 2$(I))	0.0509; 0.1204	0.0253; 0.0603	0.0429; 0.1026	0.0417; 0.1080	0.0373; 0.0947
Goodness of fit	1.282	1.346	1.331	1.429	1.154
Diffraction peak and hole (e^-/Å^3)	2.656; −1.863	2.632; −1.926	7.771; −3.765	7.323; 5.219	2.579; −3.540
Temperature (K)	300 (2)	299 (2)	301 (2)	300 (2)	301 (2)

TABLE VII. Atomic coordinates, occupancies and isotropic displacement parameters of $Mn(Pt_{1-x}Pd_x)_5P$ at 300(2) K. [U_{eq} is defined as one-third of the trace of the orthogonalized U_{ij} tensor (Å^2)].

Atom	Wyckoff.	Occ.	x	y	z	U_{eq}
			$MnPd_5P$			
Pd1	4*i*	1	0	$\frac{1}{2}$	0.2948 (1)	0.015(1)
Pd2	1*a*	1	0	0	0	0.012(2)
Mn3	1*c*	1	$\frac{1}{2}$	$\frac{1}{2}$	0	0.022(1)
P4	1*b*	1	0	0	$\frac{1}{2}$	0.016(2)
			$Mn(Pt_{0.2}Pd_{0.8})_5P$			
Pd1	4*i*	0.84(2)	0	$\frac{1}{2}$	0.29385(9)	0.0058(2)
Pt2	4*i*	0.22(2)	0	$\frac{1}{2}$	0.2948(1)	0.0058(2)
Pd3	1*a*	0.78(2)	0	0	0	0.0046(3)
Pt4	1*a*	0.22(2)	0	0	0	0.0046(3)
Mn3	1*c*	1	$\frac{1}{2}$	$\frac{1}{2}$	0	0.0128(9)
P4	1*b*	1	0	0	$\frac{1}{2}$	0.0076(11)
			$Mn(Pt_{0.4}Pd_{0.6})_5P$			
Pd1	4*i*	0.57(6)	0	$\frac{1}{2}$	0.29296(17)	0.0056(4)
Pt2	4*i*	0.43(6)	0	$\frac{1}{2}$	0.29296(17)	0.0056(4)
Pd3	1*a*	0.55(6)	0	0	0	0.0037(6)
Pt4	1*a*	0.45(6)	0	0	0	0.0037(6)
Mn3	1*c*	1	$\frac{1}{2}$	$\frac{1}{2}$	0	0.020(2)
P4	1*b*	1	0	0	$\frac{1}{2}$	0.006(2)
			$Mn(Pt_{0.5}Pd_{0.5})_5P$			
Pd1	4*i*	0.50(8)	0	$\frac{1}{2}$	0.29274(18)	0.0078(5)
Pt2	4*i*	0.50(8)	0	$\frac{1}{2}$	0.29274(18)	0.0078(5)
Pd3	1*a*	0.42(6)	0	0	0	0.0049(7)
Pt4	1*a*	0.58(6)	0	0	0	0.0049(7)
Mn3	1*c*	1	$\frac{1}{2}$	$\frac{1}{2}$	0	0.015(3)
P4	1*b*	1	0	0	$\frac{1}{2}$	0.011(3)
			$Mn(Pt_{0.6}Pd_{0.4})_5P$			
Pd1	4*i*	0.43(6)	0	$\frac{1}{2}$	0.29254(11)	0.0084(6)
Pt2	4*i*	0.57(6)	0	$\frac{1}{2}$	0.29254(11)	0.0084(6)
Pd3	1*a*	0.38(6)	0	0	0	0.0068(7)
Pt4	1*a*	0.62(6)	0	0	0	0.0068(7)
Mn3	1*c*	1	$\frac{1}{2}$	$\frac{1}{2}$	0	0.012(3)
P4	1*b*	1	0	0	$\frac{1}{2}$	0.014(4)

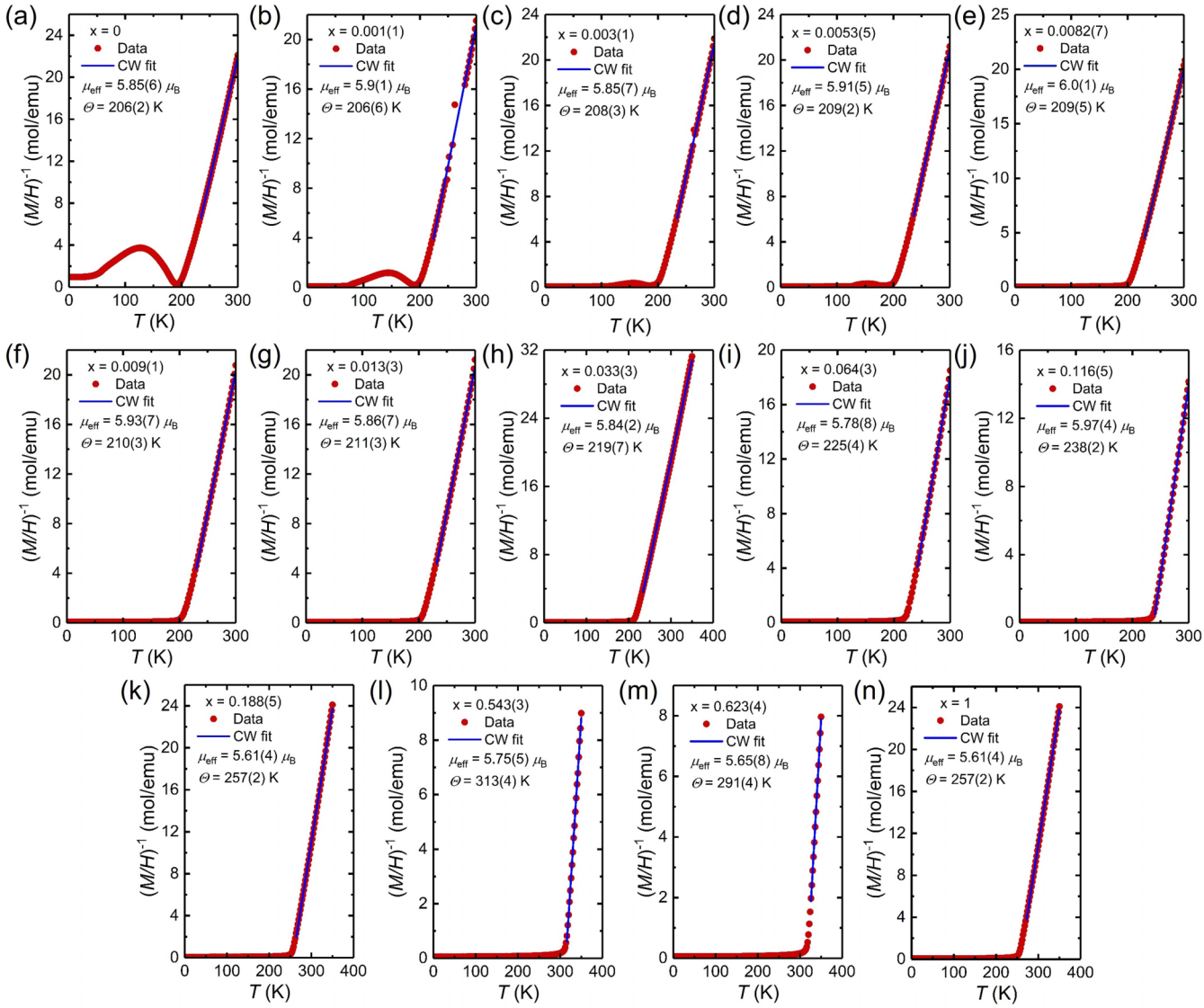

FIG. 10. Polycrystalline averaged $(M/H)^{-1}$ for the single-crystal $Mn(Pt_{1-x}Pd_x)_5P$ samples measured at $H = 1$ kOe [M/H shown in Figs. 5(a) and 5(b) in the main text]. All samples show Curie-Weiss behavior above the respective magnetic transition temperatures.

ferromagnetic ordering. That the Weiss temperature of pure $MnPt_5P$ ($x = 0$) is also positive, despite ordering antiferromagnetically, likely points to the close proximity of this phase to ferromagnetic order. The effective moments, μ_{eff}, estimated from the fitted Curie constants, remain effectively constant at $\approx 5.8\mu_B$ across the substitutions series, in excellent agreement with $5.9\mu_B$, which is theoretically anticipated for Mn^{2+} moments.

4. Magnetic data for polycrystalline $Mn(Pt_{1-x}Pd_x)_5P$

Because the crystallographic data for $MnPd_5P$ and $Mn(Pt_{1-x}Pd_x)_5P$ was obtained from small single crystals picked from solid-state reactions, we also measured the magnetic properties of the sintered pellets to ensure consistency with the solution-grown single crystals discussed in the main text. The magnetic properties of the polycrystalline $Mn(Pt_{1-x}Pd_x)_5P$ ($x = 0.2$, 0.4, 0.5, 0.6, 0.8, and 1) were measured in a Quantum Design PPMS Dynacool (QD-PPMS) at the National High Magnetic Field Laboratory over a temperature range of 1.8 to 400 K with the applied field of 1 kOe. Additionally, magnetic measurements of Pt doped compounds were carried out in a vibrating sample magnetometer (VSM) in a Quantum Design PPMS system over a temperature range of 1.8–600 K with the applied field of 1 kOe. The field dependent magnetization measurements were carried out at several different temperatures between 2–350 K and in fields up to 90 kOe.

The magnetic data for the polycrystalline $Mn(Pt_{1-x}Pd_x)_5P$ samples are displayed in Figs. 11 and 12. Like the single crystals discussed above, the Pd-containing polycrystalline samples, which have $0.2 \geqslant x \geqslant 1$, also show ferromagnetic

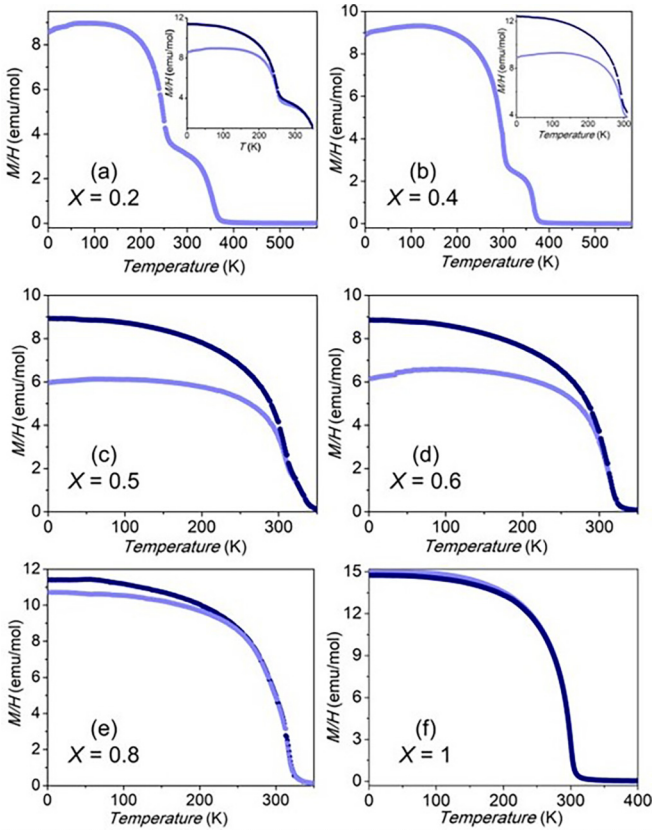

FIG. 11. Temperature-dependent M/H measured on pellets of polycrystalline $Mn(Pt_{1-x}Pd_x)_5P$.

behavior where T_C is maximized near 312 K for $\approx x = 0.60$ Pd. However, in addition to the $Mn(Pt_{1-x}Pd_x)_5P$ primary phase, the polycrystalline pellets also contained a small fraction of a ferromagnetic impurity, likely $MnPt_3$ ($T_C \approx 390$ K) [38,39]. Owing to the strong response of ferromagnetism to an applied magnetic field, even small ferromagnetic impurities are easily detected in magnetization measurements, and our polycrystalline samples with $x < 0.5$ all show high-temperature ($T > 300$ K) ferromagnetic-like transitions that are not observed in any of the datasets collected on the single crystals. An analogous $MnPd_3$ phase also exists, but orders antiferromagnetically [40–42], which likely explains why the polycrystalline $Mn(Pt_{1-x}Pd_x)_5P$ samples with $x > 0.5$ do not show evidence for a second transition. As the ordering of $MnPt_3$ could easily be misinterpreted as a second, higher temperature, transition in the Pt-rich samples, the contrast between single and polycrystalline data is an excellent demonstration of the advantages of solution growth, which allows us to produce high quality $Mn(Pt_{1-x}Pd_x)_5P$ crystals free of significant contamination by magnetic impurities. The field-dependent magnetization isotherms for the polycrystalline samples are shown in Fig. 12 and show soft ferromagnetic behavior below T_1 and saturated moments $\approx$4–4.5μ_B/f.u. at 2 K. Excluding the transitions from the $MnPt_3$, the intrinsic Curie temperatures of the polycrystalline samples are otherwise in good agreement with those inferred from the data collected on single crystals.

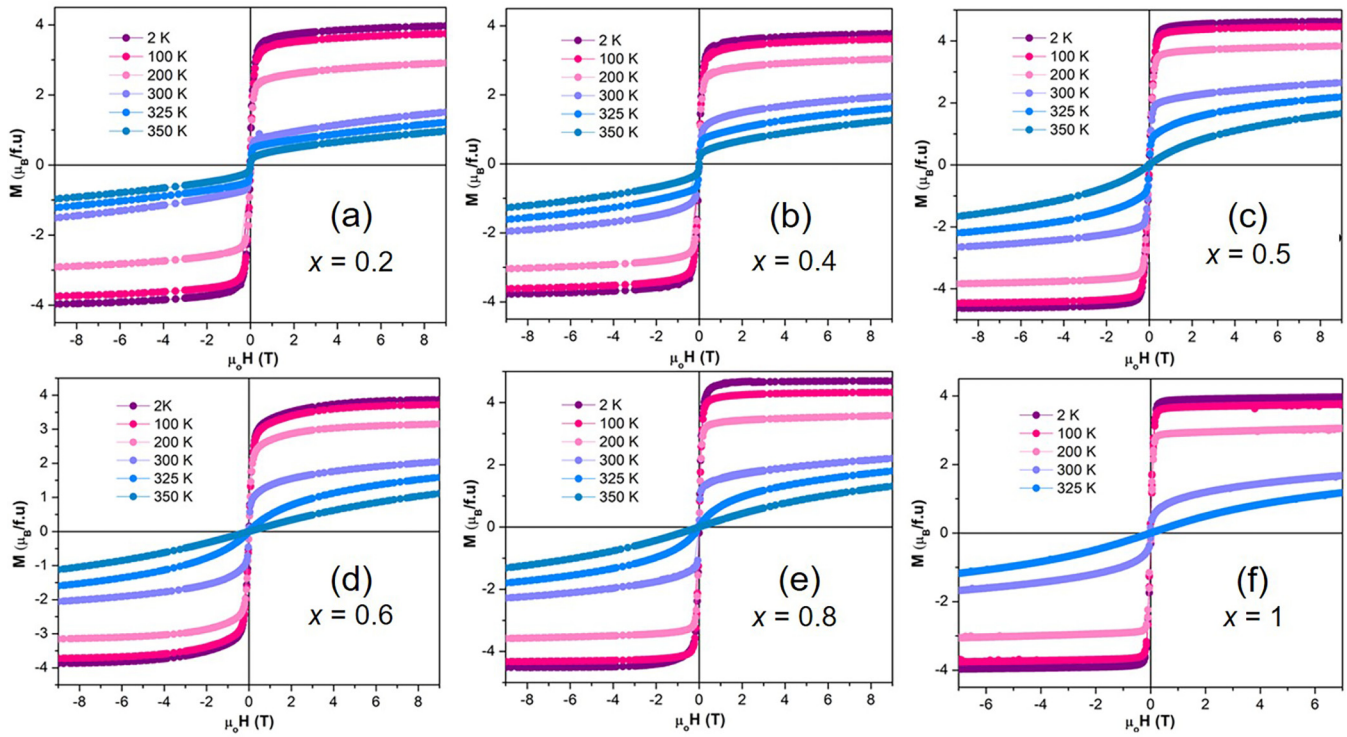

FIG. 12. Field-dependent magnetization isotherms measured on pellets of polycrystalline $Mn(Pt_{1-x}Pd_x)_5P$.

[1] T. Dietl, A ten-year perspective on dilute magnetic semiconductors and oxides, Nat. Mater. **9**, 965 (2010).

[2] J. B. Goodenough, Direct cation–cation interactions in several oxides, Phys. Rev. **117**, 1442 (1960).

[3] G. D. Samolyuk and G. J. Miller, Relation between chemical bonding and exchange coupling approaches to the description of ordering in itinerant magnets, J. Comput. Chem. **29**, 2177 (2008).

[4] J. M. Santiago, C. L. Huang, E. Morosan, Itinerant magnetic metals, J. Phys.: Condens. Matter **29**, 373002 (2017).

[5] Z. Fei, B. Huang, P. Malinowski, W. Wang, T. Song, J. Sanchez, W. Yao, D. Xiao, X. Zhu, A. F. May *et al.*, Two-dimensional itinerant ferromagnetism in atomically thin Fe_3GeTe_2, Nat. Mater. **17**, 778 (2018).

[6] Y. Zhang, G. J. Miller, and B. P. Fokwa, Computational design of rare-earth-free magnets with the $Ti_3Co_5B_2$-type structure, Chem. Mater. **29**, 2535 (2017).

[7] P. Shankhari, J. P. Scheifers, M. Hermus, K. Yubuta, and B. P. Fokwa, Unexpected trend deviation in isoelectronic transition metal borides $A_3T_5B_2$ (A = group 4, T = group 9): $Ti_3Co_5B_2$-vs. perovskite-type studied by experiments and DFT calculations, Z. Anorg. Allg. Chem. **643**, 1551 (2017).

[8] B. Chen, J. Yang, H. Wang, M. Imai, H. Ohta, C. Michioka, K. Yoshimura, and M. Fang, Magnetic properties of layered itinerant electron ferromagnet Fe_3GeTe_2, J. Phys. Soc. Jpn. **82**, 124711 (2013).

[9] B. P. T. Fokwa, H. Lueken, and R. Dronskowski, Rational design of complex borides – one-electron-step evolution from soft to semi-hard itinerant ferromagnets in the new boride series $Ti_2FeRu_{5-n}Rh_nB_2$ ($1 \leqslant n \leqslant 5$), Eur. J. Inorg. Chem. **2011**, 3926 (2011).

[10] M. El-Boragy and K. Schubert, Über eine verzerrte dichteste Kugelpackung mit Leerstellen/On a deformed close-packed structure containing constitutional vacancies, Int. J. Mater. Res. **61**, 579 (1970).

[11] X. Gui, R. A. Klein, C. M. Brown, and W. Xie, Chemical bonding governs complex magnetism in $MnPt_5P$, Inorg. Chem. (Washington, DC, US) **60**, 87 (2021).

[12] X. Gui, M. Marshall, R. S. Dissanayaka Mudiyanselage, R. A. Klein, Q. Chen, Q. Zhang, W. Shelton, H. Zhou, C. M. Brown, H. Cao, M. Greenblatt, and W. Xie, Spin reorientation in antiferromagnetic layered $FePt_5P$, ACS Appl. Electron. Mater. **3**, 3501 (2021).

[13] X. Gui and W. Xie, Crystal structure, magnetism, and electronic properties of a rare-earth-free ferromagnet: $MnPt_5As$, Chem. Mater. **32**, 3922 (2020).

[14] R. S. Dissanayaka Mudiyanselage, Q. Zhang, M. Marshall, M. Croft, Z. Shu, T. Kong, and W. Xie, Spin reorientation in antiferromagnetic $MnPd_5Se$ with an anti-$CeCoIn_5$ structure type, Inorg. Chem. (Washington, DC, US) **61**, 3981 (2022).

[15] T. J. Slade and P. C. Canfield, Use of refractory-volatile element deep eutectic regions to grow single crystalline intermetallic compounds, Z. Anorg. Allg. Chem. **648**, e202200145 (2022).

[16] P. C. Canfield, T. Kong, U. S. Kaluarachchi, and N. H. Jo, Use of frit-disc crucibles for routine and exploratory solution growth of single crystalline samples, Philos. Mag. **96**, 84 (2016).

[17] *Canfield Crucible Sets*, https://www.lspceramics.com/canfield-crucible-sets-2/, Accessed: 2022-03-23.

[18] P. C. Cafield, New materials physics, Rep. Prog. Phys. **83**, 016501 (2020).

[19] B. H. Toby and R. B. Von Dreele, GSAS-II: The genesis of a modern open-source all purpose crystallography software package, J. Appl. Crystallogr. **46**, 544 (2013).

[20] G. M. Sheldrick, Crystal structure refinement with *SHELXL*, Acta Crystallogr., Sect. C: Struct. Chem. **71**, 3 (2015).

[21] P. Muller, R. Herbst-Irmer, A. Spek, T. Schneider, and M. Sawaya, *Crystal Structure Refinement: A Crystallographer's Guide to SHELXL* (Oxford University Press, Oxford, 2006), Vol. 8.

[22] K. Momma and F. Izumi, VESTA: A three-dimensional visualization system for electronic and structural analysis, J. Appl. Crystallogr. **41**, 653 (2008).

[23] D. E. Newbury and N. W. Ritchie, Rigorous Quantitative Elemental Microanalysis by Scanning Electron Microscopy/Energy Dispersive X-Ray Spectrometry (SEM/EDS) with Spectrum Processing by NIST DTSA-II, in *Scanning Microscopies* (SPIE, 2014), Vol. 9236, pp. 90–106.

[24] P. Hohenberg and W. Kohn, Inhomogeneous electron gas, Phys. Rev. **136**, B864 (1964).

[25] W. Kohn and L. J. Sham, Self-consistent equations including exchange and correlation effects, Phys. Rev. **140**, A1133 (1965).

[26] J. P. Perdew, A. Ruzsinszky, G. I. Csonka, O. A. Vydrov, G. E. Scuseria, L. A. Constantin, X. Zhou, and K. Burke, Restoring the Density-Gradient Expansion for Exchange in Solids and Surfaces, Phys. Rev. Lett. **100**, 136406 (2008).

[27] G. Kresse and J. Furthmüller, Efficient iterative schemes for *ab initio* total-energy calculations using a plane-wave basis set, Phys. Rev. B **54**, 11169 (1996).

[28] G. Kresse and J. Furthmüller, Efficiency of *ab initio* total energy calculations for metals and semiconductors using a plane-wave basis set, Comput. Mater. Sci. **6**, 15 (1996).

[29] P. E. Blöchl, Projector augmented-wave method, Phys. Rev. B **50**, 17953 (1994).

[30] H. J. Monkhorst and J. D. Pack, Special points for Brillouin-zone integrations, Phys. Rev. B **13**, 5188 (1976).

[31] M. E. Fisher and J. S. Langer, Resistive Anomalies at Magnetic Critical Points, Phys. Rev. Lett. **20**, 665 (1968).

[32] S. Nandi, M. G. Kim, A. Kreyssig, R. M. Fernandes, D. K. Pratt, A. Thaler, N. Ni, S. L. Bud'ko, P. C. Canfield, J. Schmalian, R. J. McQueeney, and A. I. Goldman, Anomalous Suppression of the Orthorhombic Lattice Distortion in Superconducting $BaFe_{1-x}Co_xAs_2$ Single Crystals, Phys. Rev. Lett. **104**, 057006 (2010).

[33] D. D. Khalyavin, S. W. Lovesey, P. Manuel, F. Krüger, S. Rosenkranz, J. M. Allred, O. Chmaissem, and R. Osborn, Symmetry of reentrant tetragonal phase in $Ba_{1-x}Na_2Fe_2As_2$: Magnetic versus orbital ordering mechanism, Phys. Rev. B **90**, 174511 (2014).

[34] P. Muralt, R. Kind, R. Blinc, and B. Zeks, Incommensurate-Reentrant High-Symmetry Phase Transition in a Layer-Structure Perovskite, Phys. Rev. Lett. **49**, 1019 (1982).

[35] M. Saura-Múzquiz, F. P. Marlton, B. G. Mullens, A. M. Manjón-Sanz, J. C. Neuefeind, M. Everett, H. E. Brand, S. Mondal, G. Vaitheeswaran, and B. J. Kennedy, Understanding the re-entrant phase transition in a non-magnetic scheelite, J. Am. Chem. Soc. **144**, 15612 (2022).

[36] J. F. Khoury, A. J. Rettie, I. Robredo, M. J. Krogstad, C. D. Malliakas, A. Bergara, M. G. Vergniory, R. Osborn, S. Rosenkranz, D. Y. Chung *et al.*, The subchalcogenides

Ir_2In_8Q (Q = S, Se, Te): Dirac semimetal candidates with re-entrant structural modulation, J. Am. Chem. Soc. **142**, 6312 (2020).

[37] P. Schobinger-Papamantellos, J. Rodriguez-Carvajal, G. André, and K. Buschow, Re-entrant ferrimagnetism in $TbMn_6Ge_6$, J. Magn. Magn. Mater. **150**, 311 (1995).

[38] B. Antonini, F. Lucari, F. Menzinger, and A. Paoletti, Magnetization distribution in ferromagnetic $MnPt_3$ by a polarized-neutron investigation, Phys. Rev. **187**, 611 (1969).

[39] B. Antonini, M. Felici, and F. Menzinger, Spin waves and exchange interactions in $MnPt_3$ ferromagnetic alloy, Phys. Lett. A **30**, 310 (1969).

[40] H. Sato and R. Toth, Long-period superlattice Pd_3Mn II and its large tetragonal distortion, Phys. Rev. **139**, A1581 (1965).

[41] E. Kre'n and G. Ka'da'r, Crystal and magnetic structures in the Mn-Pd system near $MnPd_3$, Phys. Lett. A **29**, 340 (1969).

[42] E. Krén, G. Kádár, and M. Márton, Neutron diffraction study of the $MnPd_3$ phase, Solid State Commun. **10**, 1195 (1972).